

Characteristics of Malacca Strait Throughflow during Indian Ocean Dipole mode 2020–2024

Noir P. Purba^{1,2,*}, Martono³, Ghelby M. Faid², Hind Azidane⁴, Raffy R. Alfarez², Muhammad H. Ilmi², Noor C.D. Aryanto⁵

Abstract

The hydrographic dynamics of the Malacca Strait Throughflow (MST) during Indian Ocean Dipole (IOD) events remain poorly characterized, particularly for recent years. This study investigates the characteristics of water masses and circulation from 2020 to 2024 during different IOD phases. High-resolution ocean model data from Copernicus Marine Service (CMEMS) model outputs were examined using statistical analyses of temperature, salinity, and oxygen variability, complemented by volume transport and Lagrangian simulations to examine circulation pathways. The result revealed a strong north-south gradient in water-mass properties, where the northern region is significantly affected by Andaman Sea waters, which are higher in salinity and oxygen-depleted. The southern region receives water from the Java Sea and the South China Sea, which are warmer and less saline. The middle region serves as a mixing zone between the northern and southern water masses. Seasonal variations are most evident in surface waters, whereas deep-water characteristics remain stable throughout the seasons. Evidence indicates that different mixing processes occur in each region, affecting the distribution of water properties. IOD phases significantly modulate MST conditions. The positive IOD phases result in warmer temperatures, lower oxygen levels, and more stable salinity due to decreased freshwater input. In contrast, negative phases lead to cooler temperatures, higher oxygen concentrations, and lower salinity due to increased rainfall and runoff. Crucially, particle tracking revealed a bifurcated flow, with pathways towards both the Andaman Sea and the Java Sea, and volume transport increased by 7.02% in the south during positive IOD. These findings highlight the MST's complex and regionally heterogeneous response to climate variability.

Keywords

Water mass stability; Rupert Strait; T-S diagram; Surface currents; Indonesian throughflow

¹Faculty of Fishery and Marine Science, Department of Marine Science, Universitas Padjadjaran, Bandung, Indonesia

²KomitmenX Research Group, Universitas Padjadjaran, Bandung, Indonesia

³Research and Innovation Agency (BRIN), Jakarta, Indonesia

⁴Faculty of Sciences, Department of Geology, Ibn Tofail University, Kénitra, Morocco

⁵Research Centre for Geological Resources, National Research and Innovation Agency (BRIN), Bandung, Indonesia

*Correspondence: noir.purba@unpad.ac.id (N. P. Purba)

Received: 17 September 2025; revised: 17 December 2025; accepted: 23 February 2026

1. Introduction

The Malacca Strait Throughflow (MST) serves as a crucial oceanographic connection between the Andaman Sea, Indonesian Seas, and the southern South China Sea (sSCS) (Ai et al., 2024; Daryabor et al., 2015). This complex system is shaped by dynamic interactions among monsoonal winds, tidal forces, and inter-oceanic exchanges, which influence its physical and biogeochemical characteristics, particularly salinity, temperature, and circulation patterns. In addition to seasonal variations, large-scale climate phenomena such as the El Niño-Southern Oscillation (ENSO)

and the Indian Ocean Dipole (IOD) cause significant variability in hydrographic conditions in the MST (Soumya et al., 2015). While ENSO is a coupled ocean-atmosphere mode originating in the tropical Pacific Ocean, characterized by alternating warm (El Niño) and cold (La Niña) phases that modify regional wind patterns, precipitation, and ocean circulation, the IOD is a dominant mode of interannual climate variability in the tropical Indian Ocean, defined by an east-west sea surface temperature gradient between the western and eastern basins (Saji et al., 1999; Webster et al., 1999). Despite its importance in regional water dynamics and global circulation patterns, studies on temperature and salinity variability and response to recent IOD events remain limited (Purba et al., 2018).

Recent studies have significantly refined our understanding of the regional circulation mechanism governing the MST. It is now well-established that the strait exhibits a complex, seasonally reversing circulation pattern (Roseli et al., 2015). The influence of the South China Sea and the Andaman Sea, which fluctuate between the monsoon seasons, has been emphasized by recent studies that have brought to light significant hydrographic patterns in the MST (Ibrahim, Z. Z., and Yanagi, 2006; Khoirunnisa et al., 2017). Building on this, recent high-resolution modeling and Lagrangian analyses have revealed a persistent bifurcation of the throughflow, with one branch directed north-westward toward the Andaman Sea and another south-eastward toward the Java Sea, a dynamic crucial for understanding connectivity and water mass distribution (Ai et al., 2024; Haditjar et al., 2019). During the Northeast Monsoon (December–February), strong southward currents carry high-salinity Andaman waters into the MST, increasing salinity in middle region. Conversely, during the Southwest Monsoon (June–August), the flow reverses, and low-salinity, warmer waters from the Java Sea intrude into the southern MST. This change in the flow affects the gradients of temperature and salinity (Daryabor et al., 2016). In addition, the region is strongly influenced by strong tidal currents, seasonal monsoons, river discharge, and inter-oceanic exchanges between the Pacific and Indian Oceans (Kok et al., 2021; Liu et al., 2020). The complex interplay of these forces creates a highly stratified water column, with recent research highlighting its sensitivity to climate variability (Wibowo et al., 2022).

The sea surface temperature (SST) in the MST ranges from 27.0°C to 30.0°C, with monsoonal conditions influencing this temperature (Liu et al., 2020; Roseli et al., 2015). Temperatures can drop to as low as 19°C in deeper areas of the sea (Rizal et al., 2012). The temperature in the southeastern is slightly lower, around 27.5°C, due to the effects of the South China Sea and river runoff. Meanwhile, the temperature in the northwestern reaches approximately 30°C, which is warmer because of the influence of the Andaman Sea. A thermocline, which marks the transition between the warmer surface layer and cooler waters below, is often observed at depths of 50 to 100 meters (Amiruddin M. et al., 2011). Salinity fluctuates significantly throughout the year, with the lowest surface salinity during the northeast monsoon and the highest during the southwest monsoon (Peralta and Yusoff, 2014). Salinity in the Andaman Sea varies from about 31.5 PSU near Malaysia and Sumatra, areas affected by rivers, to around 34 PSU in offshore waters (Liu et al., 2020; Rizal et al., 2012). The middle region has higher salinity due to high-salinity inflows from the Andaman Sea driven by the northeast monsoon. Conversely, the southwest monsoon brings more freshwater from rainfall and river runoff, which lowers salinity levels, especially near the shore (Amiruddin et al., 2011). The boundary between the saltier deep water and the fresher surface water

features a well-defined halocline, typically found at depths of 50 to 120 meters (Rizal et al., 2012).

To date, the majority of studies on hydrographic variability in the MST have relied on satellite data. This information, although valuable, offers limited insights into the dynamics of the subsurface. The majority of the research that has been previously conducted has been on tidal dynamics, the transportation of sediment, and monsoonal effects (Ibrahim and Yanagi, 2006; Soumya et al., 2015). However, a critical knowledge gap remains regarding the three-dimensional response of water mass structure and Lagrangian transport pathways to interannual climate forcing, particularly during recent and pronounced IOD events. This study addresses this gap by analyzing seasonal and interannual variability in temperature, salinity, and particle trajectories during different IOD phases from 2020 to 2024. In light of the absence of high-resolution in situ oceanographic data in this region, our research conducts a critical evaluation of the variability of seawater, adding to regional ocean modeling efforts, future climate impact studies, and sustainable management of marine resources in the MST. The findings will provide valuable insights into the role of IOD-driven oceanic processes in shaping the hydrography of the Malacca Strait. This will subsequently improve the accuracy of climate impact assessments and marine resource management.

2. Material and methods

2.1 Geographic features and characteristics

The MST is bordered by Peninsular Malaysia to the east and Sumatra, Indonesia, to the west, with its northern part connecting to the Andaman Sea, spanning a longitude range of 95.8°E to 105°E and a latitude range from 9°N to 2°S (Figure 1). The bathymetry of this region is complex, characterized by a shallow, narrow basin with an average depth of approximately 100 m, transitioning from steep, deep gradients in the north to shallower sections (10 to 60 m) in the middle and southern areas. The southern region is characterized by silty sand, while the middle Malacca Strait is composed of coarse-grained sediments. Seasonal cyclonic eddies and southward currents during the Southwest Monsoon (SWM) contribute to sediment redistribution. Furthermore, in the northern area, sediments are predominant, transported by monsoonal currents, tides, and waves (Ai et al., 2024). The tidal currents in the Malacca Strait are primarily influenced by semidiurnal variations, with the primary component being the M2 tide, which has a period of 12 hours (Chen et al., 2014).

The bathymetry of the Malacca Strait is defined by a shallow and narrow channel, with depths mainly under 100 m. The shallowest areas are located around the coastal zones of Malaysia and Sumatra, with certain spots, especially in the southern half adjacent to the Riau Archipelago, reaching depths of less than 25 m. Conversely, adjacent to the Andaman Sea, the northwestern section of the strait

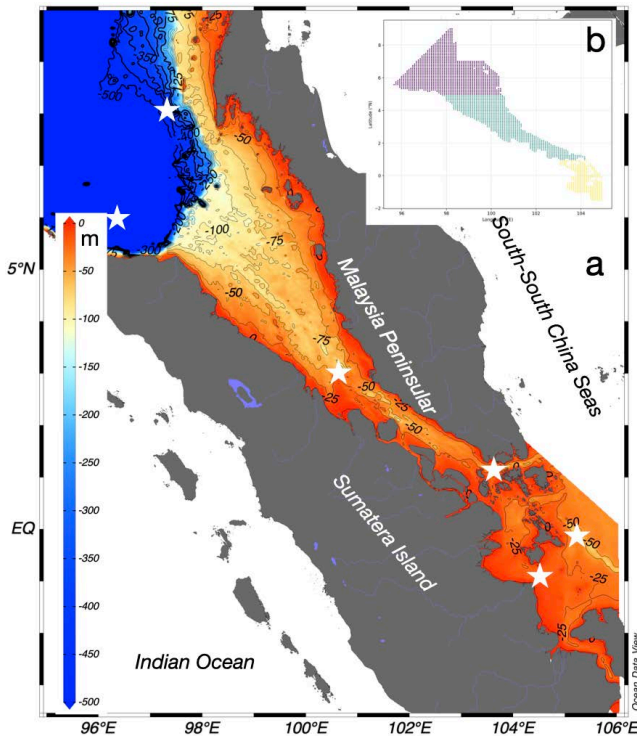


Figure 1. The geographic map of the Malacca Strait shows a) bathymetry and the two largest surrounding islands and b) the three areas for analysis. Six initial points (White stars) are chosen to simulate the ocean current pathways. The bathymetry data were provided by GEBCO with a 1/2-arc resolution

possesses a markedly deeper basin over 500 m. This profound basin creates a vital link to the Indian Ocean and enables significant water flow between the Andaman Sea and the Malacca Strait. The depth increasingly ascends from the southeastern area of the strait to the northwest in the Andaman Sea, creating a smooth gradient, while the middle portion of the strait displays intermediate depths of 50 to 150 m.

2.2 Data and method

The primary aim of this study is to examine the water mass in the Malacca Strait from 2020 to 2024, focusing on seasonal and monthly fluctuations. The primary data for this study were obtained from the Copernicus Marine Environment Monitoring Service (CMEMS). These data consist of Level-4 numerical ocean model reconstructions that assimilate satellite remote-sensing observations and available in-situ measurements, producing a consistent, gap-free representation of the ocean state. This dataset includes temperature, salinity, current velocity, and sea level height, with a horizontal resolution of $1/12^\circ$ (~ 8 km). The dataset covers the period from November 1, 2020, to February 21, 2025, with data accessible at hourly, daily, and monthly intervals. It encompasses up to deep layers, offering insights

into vertical oceanic structures, and is ideal for analyzing oceanographic variability in data-sparse regions like the Malacca Strait. The dataset is refreshed daily at 12:00 UTC and on the 15th of each month at 12:00 UTC for monthly updates. The data is available in NetCDF-3 and NetCDF-4 formats, guaranteeing compatibility with diverse analytical tools.

The secondary purpose of this study is to examine circulation using a specific analysis method. To complement the Eulerian current analysis and directly investigate the connectivity and pathways of water masses within the strait and to adjacent seas, we performed Lagrangian particle tracking simulations using OceanParcels v. 3.10.12 (<https://oceanparcels.org>). The northward (V) and eastward (U) current velocity from the CMEMS model outputs was used as the basis for particle movement analysis in the study area. The spatial resolution of the data used is $0.083^\circ \times 0.083^\circ$ with a temporal resolution from January 1, 2020, to December 1, 2024. When single-depth modelling was performed, this data was filtered at that single depth to prevent the algorithm from executing modelling at other depths.

The six Initial Points (IPs) were selected to represent key inflow and outflow regions of the Malacca Strait (Andaman Sea, Java Sea, Singapore Strait) and its central axis, allowing assessment of long-term circulation pathways and connectivity using Lagrangian particle tracking. Their locations were as follows: two IPs were placed in the southeast, near the Riau Islands, to track flow towards the Java Sea; two IPs were placed in the northwest, near the transition to the Andaman Sea; one IP was placed in the middle strait; and one IP was placed near the Singapore Strait. This configuration was designed to capture the major exchange pathways. Particle movement modelling was performed for 1,797 days (five years) from January 1, 2020, releasing one particle every 24 hours from each IP. A timestep of 24 hours was selected to ensure computational efficiency for the five-year simulation period while being sufficient to resolve the dominant, large-scale advective processes. Each released particle was treated separately. By default, particles may become trapped at land boundaries where velocity fields are undefined. To avoid this case, 'freeslip' interpolation was used so that each land boundary would 'push' particles that approach it based on U and V data around the land boundary. The timestep used in this modelling was 24 hours, meaning each particle's position was calculated every 24 hours. This method is designed to identify the 'mean pathways and connectivity' over the long term. Time extrapolation was employed to reconcile the discrepancies between the time steps of the data and those of the modeling process.

As explained by Lange and van Sebille (2017), in Lagrangian modelling, particle pathway calculations use the

following formula:

$$X(t + \Delta t) = X(t) + \int_t^{t+\Delta t} v(x, \tau) d\tau + \Delta X_b(t) \quad (1)$$

where $X(t)$ is the position of the particle in three dimensions, $v(x, \tau)$ is the velocity value at a particular location obtained from the Ocean General Circulation Model (OGCM), and $\Delta X_b(t)$ is the change in position caused by certain factors, such as negative buoyancy, which cause the particle to move vertically.

2.3 Data quality control

The data cleaning procedure encompassed several stages to ensure both reliability and quality. Initially, rows without temperature and depth information were discarded to remove incomplete observations. Subsequently, temperatures below -2°C and above 40°C were excluded, retaining only plausible oceanographic data. Negative depth values were eliminated to ensure uniformity within the dataset. Approximately 49% of salinity values are missing from the dataset, limiting the dataset's comprehensiveness. A significant portion of salinity data points were flagged as missing in the raw model output for certain grid cells and depths, particularly in shallow coastal regions where the model may not compute values. Our quality control procedure focused on the available, model-validated data. The subsequent filtering for implausible values was applied to this subset, ensuring the final dataset used for analysis was robust and physically realistic. Furthermore, implausible salinity values were eliminated to guarantee data precision, preserving only those within the 20–40 PSU range. This ensures that the residual salinity data is both realistic and dependable for analysis. The majority of ocean current data (85.6%) is obtained from the upper 50 m of the water column, underscoring the predominance of current observations in the surface layer.

The northern region displays the most extensive temperature variation (6.60 to 33.31°C) and the lowest average temperature ($26.71 \pm 6.46^\circ\text{C}$). The middle and southern regions have elevated and more consistent mean temperatures, approximately 30°C , with reduced standard deviations, signifying more homogeneous thermal conditions. The northern section exhibits the highest mean salinity at 32.73 ± 1.39 PSU. The southern region exhibits the lowest salinity values, with a mean of 31.14 ± 0.88 PSU. The southern region has the highest average concentration of dissolved oxygen ($197.11 \pm 26.61 \mu\text{mol m}^{-3}$), while the northern region displays the lowest average concentration ($161.78 \pm 66.01 \mu\text{mol m}^{-3}$) and the most significant variability (Table 1).

A conservative $3 \times \text{IQR}$ threshold was applied to identify and remove only the most extreme statistical outliers, which were considered non-physical artifacts, thereby preserving the natural variability of the oceanographic data. This approach classified any data point over three times

the IQR beyond the first quartile (Q1) or third quartile (Q3) as an outlier. The interquartile range (IQR) signifies the middle 50% of the data, whereas extreme values beyond this interval were either eliminated or addressed appropriately. After subsetting the global dataset to the study area and applying all quality control filters, approximately 44.73% of the initial data points within the domain were retained.

$$[Q1 - 3 \times \text{IQR}, Q3 + 3 \times \text{IQR}] \quad (2)$$

The cleaned dataset exhibits a temperature range from 24.28°C to 34.98°C , with a mean temperature of 29.84°C . The data demonstrates strong consistency, as indicated by a relatively small standard deviation of 1.09°C . Additionally, the dataset reveals a clear thermal stratification pattern with depth, characteristic of tropical ocean waters, as suggested by the observed temperature range.

2.4 Analysis

A comprehensive statistical approach examined the relationship between Indian Ocean Dipole (IOD) phases and oceanographic parameters. In-situ temperature was converted to potential temperature (θ) using the GSW Oceanographic Toolbox to remove the compressibility effect of pressure, allowing for a direct and accurate comparison of the thermal properties of water masses at different depths. The GSW is a scientific software toolset utilized in oceanography for the precise computation of seawater parameters. It was developed as part of the TEOS-10 standard, which stands for Thermodynamic Equation of Seawater 2010. GSW calculates Theta using iterative thermodynamic equations rather than simple empirical fits (McDougall and Barker, 2011).

$$\theta = \theta(S_A, T, p, pref) \quad (3)$$

where S_A = absolute salinity (g kg^{-1}); T = in-situ temperature ($^\circ\text{C}$); p = measured pressure (dbar); $pref$ = reference pressure (typically 0 dbar).

Volume transport was calculated across defined transects in the northern, middle, and southern regions of the strait. The cross-sectional area for each transect was computed based on the GEBCO bathymetry data and the chosen depth layers. We applied a depth-dependent velocity model with five standard oceanographic data layers: surface (0–50 m), subsurface (50–100 m), intermediate (100–200 m), deep (200–500 m), and bottom (500–1000 m). A velocity attenuation model was employed, wherein velocity diminishes with depth, and the computed volume transfer was derived using the formula:

$$\text{Volume Transport (Sv)} = \text{Velocity (m/s)} \times \text{Cross-sectional Area (m}^2\text{)} / 10^6 \quad (4)$$

Table 1. Data statistics in each region

No.	Parameters	Region		
		northern region	middle region	southern region
1	temperature range (°C)	6.60 to 33.31	17.29 to 35.24	27.55 to 34.29
2	salinity range (PSU)	27.08 to 35.27	25.96 to 34.84	24.67 to 32.89
3	oxygen range ($\mu\text{mol m}^{-3}$)	2.23 to 230.69	1.30 to 223.99	31.75 to 234.90
4	temperature mean \pm std (°C)	26.71 ± 6.46	30.20 ± 1.17	30.03 ± 0.88
5	salinity mean \pm std (PSU)	32.73 ± 1.39	31.50 ± 0.98	31.14 ± 0.88
6	oxygen mean \pm std ($\mu\text{mol m}^{-3}$)	161.78 ± 66.01	194.86 ± 34.63	197.11 ± 26.61

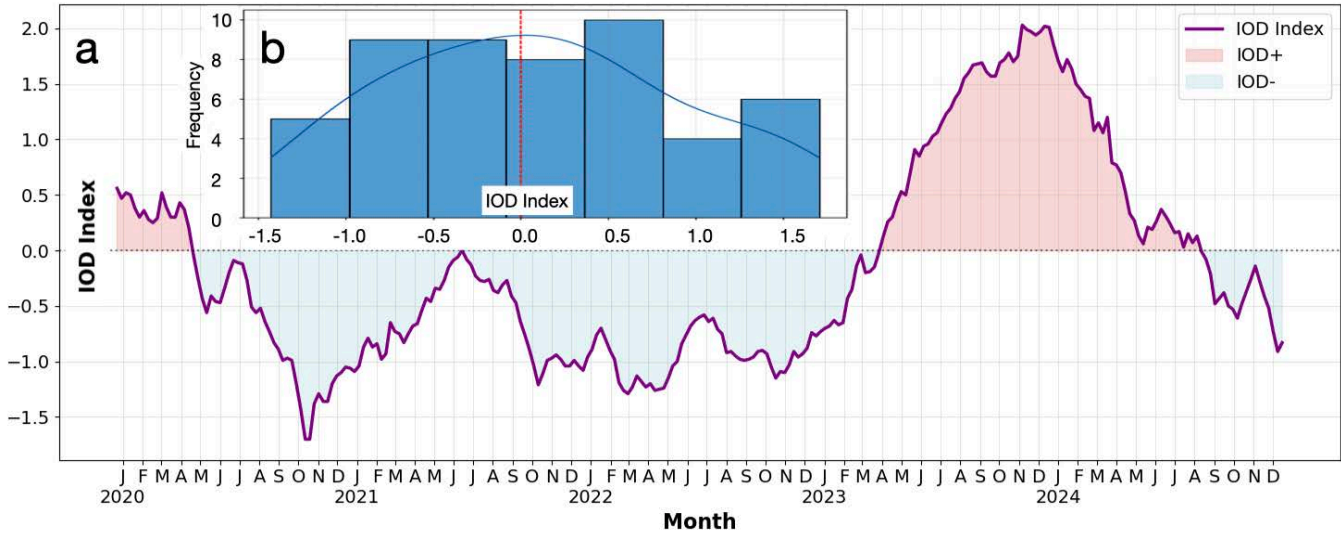


Figure 2. a) The IOD index from 2020 to 2024, where the red shaded areas represent IOD positive, while the blue shaded regions represent IOD negative. b) The frequency of IOD+ periods (28 months) and IOD- periods (23 months).

The oceanographic conditions were assessed in relation to the IOD to investigate the impact of large-scale climate variability. Time-series data on temperature, salinity, and current profiles were analyzed in relation to established IOD phases to discern patterns and anomalies linked to positive or negative occurrences, which are recognized to influence water circulation and thermohaline structure in the region substantially (Figure 2). A comparative statistical analysis was performed to assess the differences among these phases. This encompassed independent t-tests to ascertain statistically significant differences ($p < 0.05$), percent change computations to measure the extent of variance, and descriptive statistics (mean and standard deviation) for each parameter throughout both IOD phases. Pearson correlation analysis was utilized to examine the correlations between the IOD index and oceanographic factors, providing correlation coefficients (r) and corresponding p-values.

Between 2020 and 2022, primarily adverse IOD conditions were observed, with 2022 representing the most consistently unfavourable year (mean: -0.958 , std: 0.197). Conversely, 2023 and 2024 exhibited a transition to primarily positive IOD conditions, with 2023 recording the

highest mean IOD value (0.812) and the greatest variability (std: 0.933). The most intense positive IOD event occurred in November 2023 ($+2.030$), whereas the most severe negative IOD event occurred in October 2020 (-1.700). In 2024, the IOD exhibited a favourable trend, accompanied by significant fluctuations.

3. Results

3.1 Distribution of water masses

The vertical distribution of water masses shows a clear north-south gradient. The proportion of surface water decreases progressively from the northern to the southern region (65.6%, 49.4%, 33.8%), while deep water increases correspondingly (28.9%, 50.1%, 66.2%) (Figure 3). This pronounced barrier signifies significant stratification between surface and deep layers, implying divergent mixing regimes at this latitude.

In the northern region, surface water dominates the upper layer, with intermediate water contributing approximately 5.5% between depths of 100 and 200 m. The middle region shows nearly equal contributions of surface and deep waters, with a minimal intermediate water ($\sim 0.4\%$)

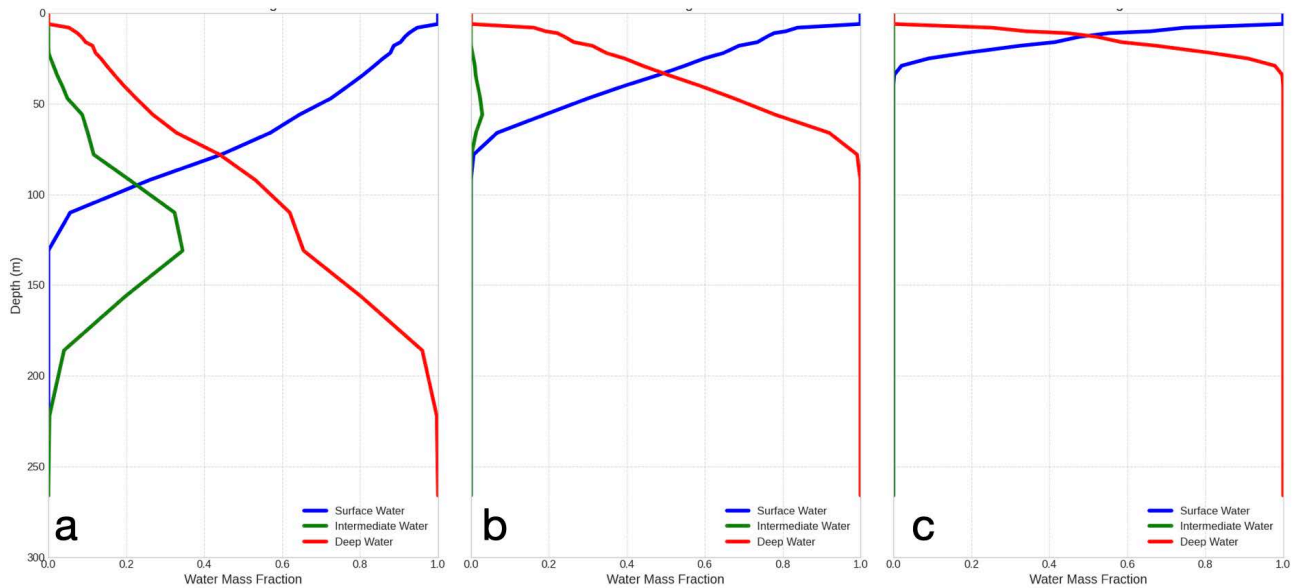


Figure 3. The vertical distribution of water masses in three regions: a) northern region, b) middle region, and c) southern region.

around 150 m. In the southern region, surface water is confined to very shallow depths, and the deep-water is dominant below 50 m.

3.2 Layer structure of temperature, salinity, and oxygen

During IOD conditions, clear regional contrasts are observed in temperature, salinity, and dissolved oxygen (Figure 4). The northern region is characterized by lower temperatures, lower oxygen concentration, and higher salinity. The middle region exhibits the highest temperatures and high oxygen concentrations with a relatively narrow distribution. The southern region shows cooler temperatures, fresher water, and higher oxygen concentration, along with greater variability in temperature and

salinity.

The middle region records the highest median temperature (~30.5°C), followed by the northern (~30.0°C) and southern regions (~29.8°C). The southern region exhibits the widest temperature range (26.0–31.0°C). Median salinity decreases southward, with the highest values in the northern region (~32.1 PSU) and the lowest in the southern region (~31.0 PSU). Dissolved oxygen shows an opposite pattern, with the lowest median values in the northern region (~170 μmol kg⁻¹) and the highest in the southern region (~260 μmol kg⁻¹).

Vertical profiles reveal strong stratification across all regions (Figure 5). Temperature decreases sharply with depth, with warm surface waters and persistently cold

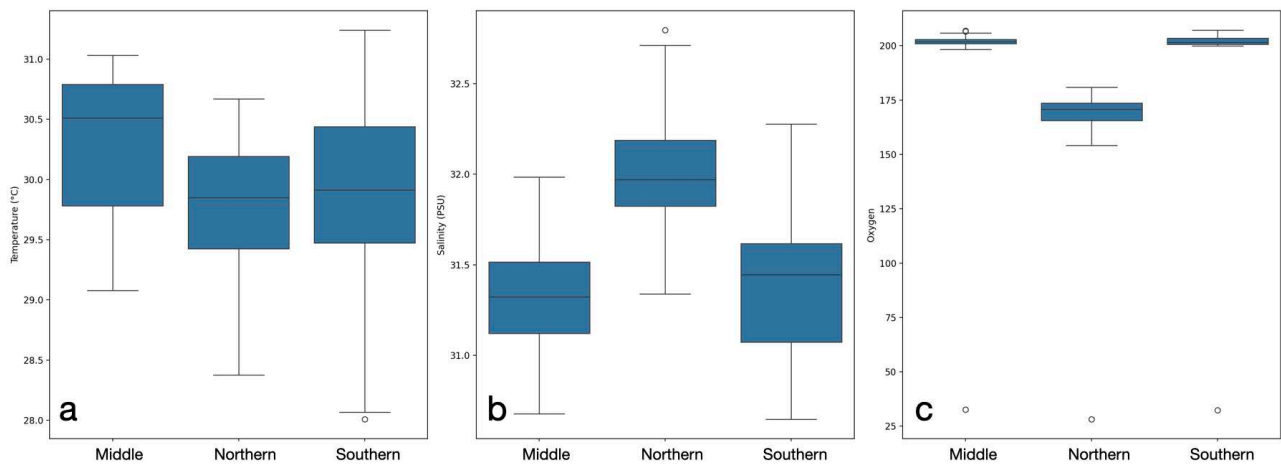


Figure 4. Three boxplots representing the distribution of a) temperature (°C), b) salinity (PSU), and c) oxygen (μmol kg⁻¹) across three regions: middle, northern, and southern parts.

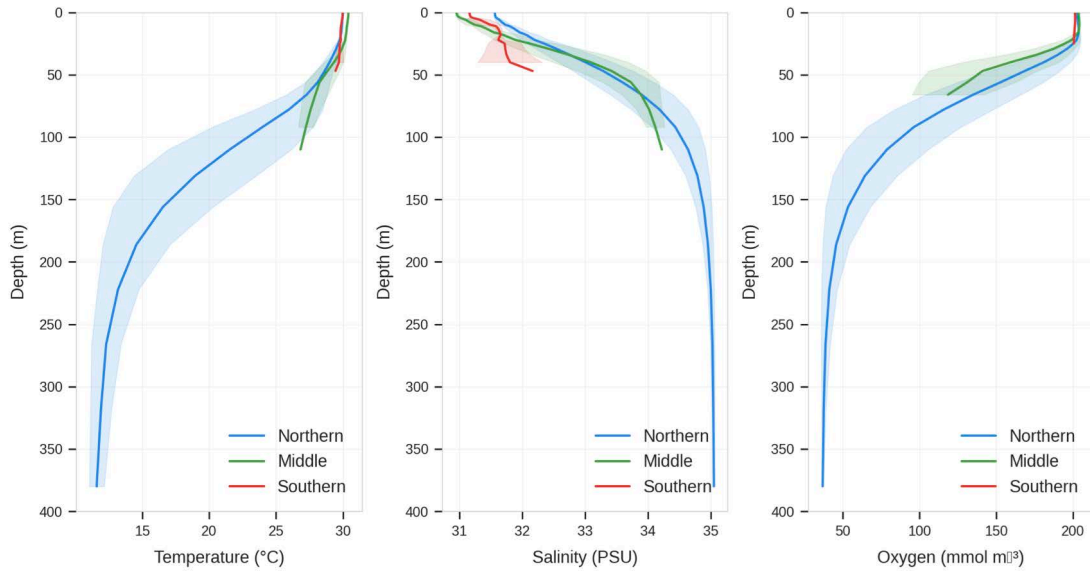


Figure 5. The vertical profile of temperature, salinity, and oxygen concentration in the three regions.

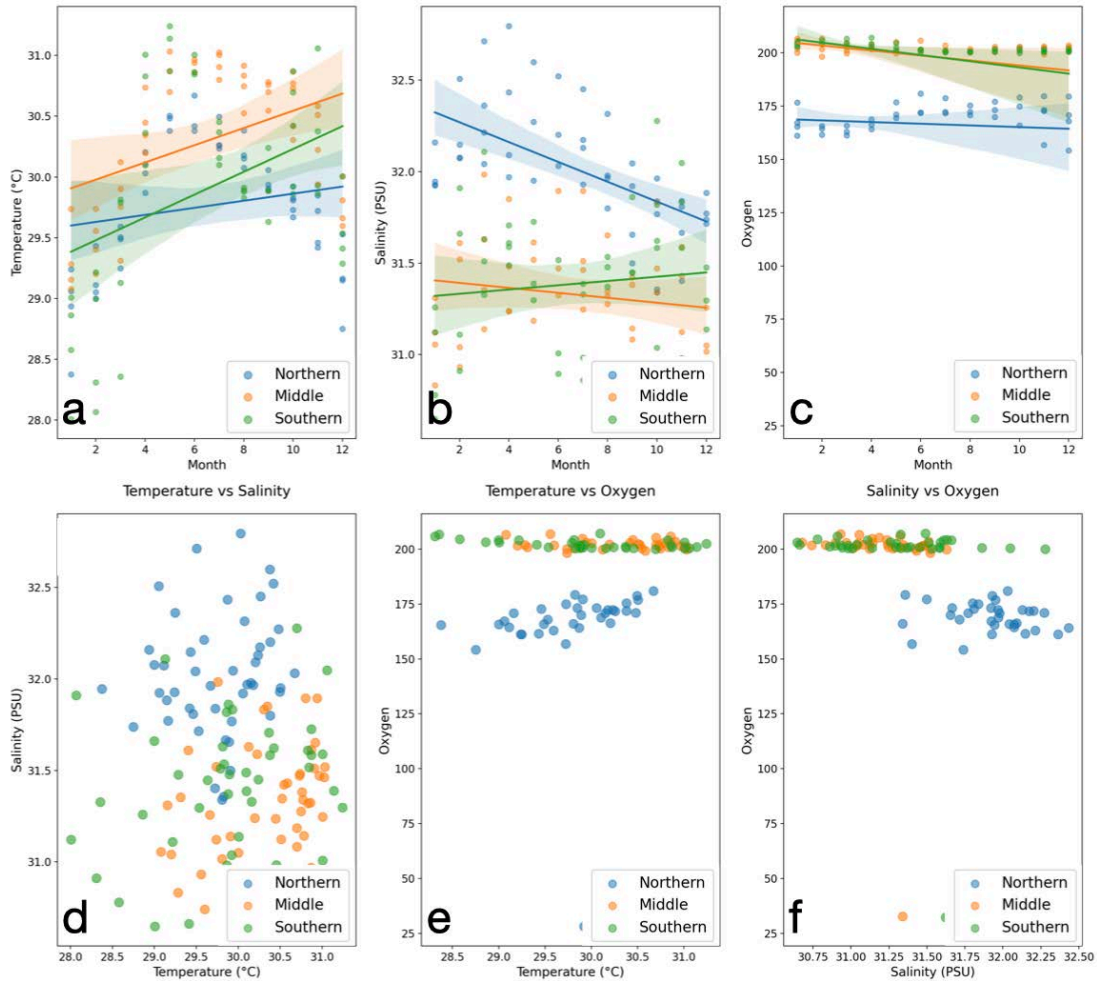


Figure 6. Monthly patterns of a) temperature, b) salinity, and c) dissolved oxygen and inter-variable relationships, d) temperature–salinity, e) temperature–oxygen, f) salinity–oxygen across three regions.

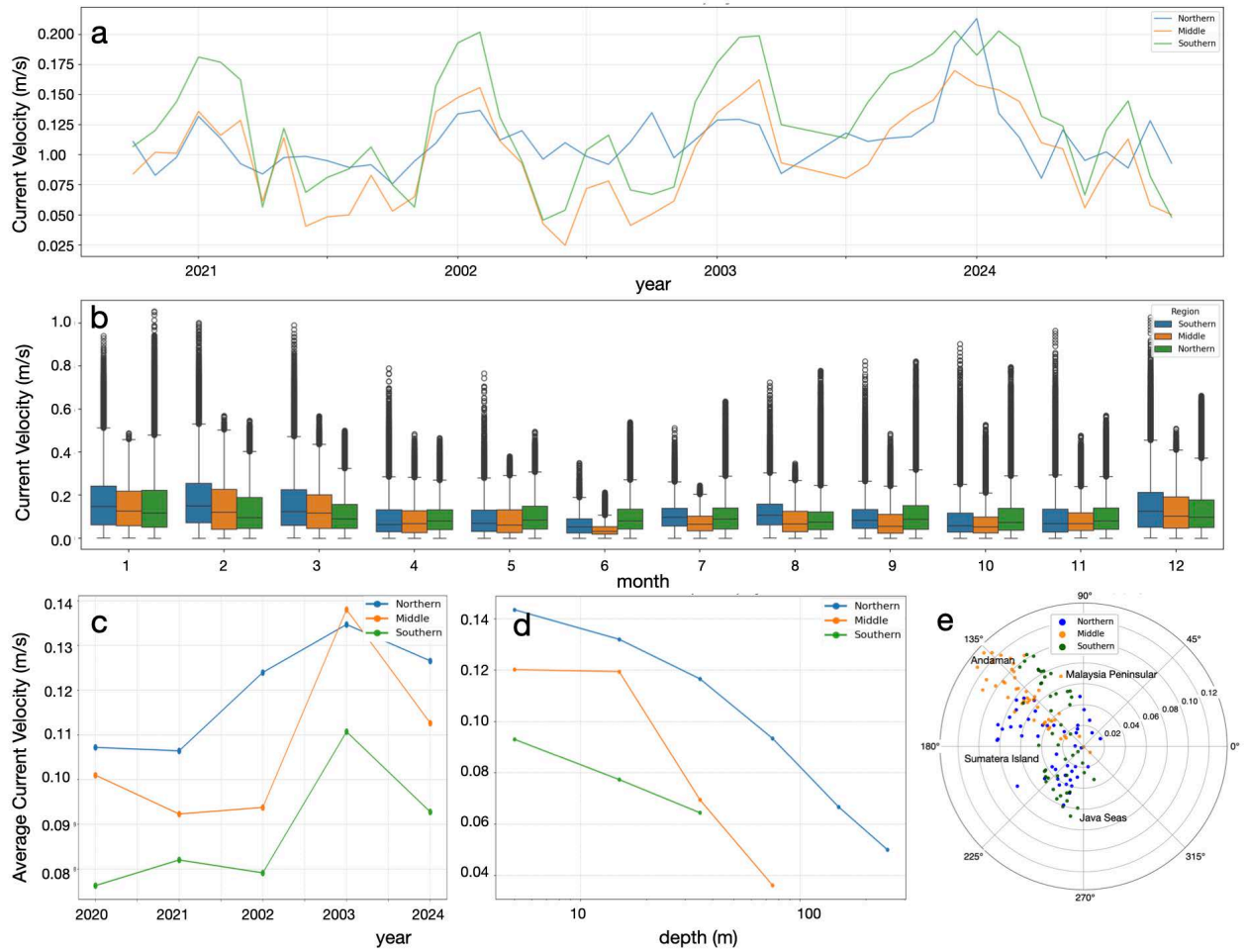


Figure 7. Comprehensive overview of ocean current dynamics across three regions of the study area, a) a time series analysis of current speed measurements for each region, highlighting continuous variations over time, b) monthly current velocity variation, c) average current velocity over the year, d) current velocity from the surface to 100 m in each region, e) current direction and velocity by region.

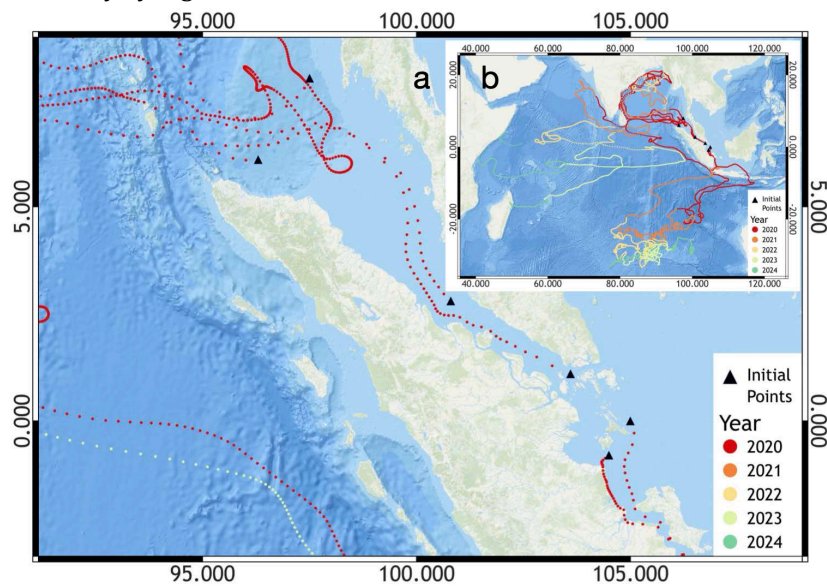


Figure 8. Particle tracking in the Malacca Strait with a) six initial points and b) enlarged areas with the African continent in the west, the Java Sea in the east, and the Indian Ocean in the south.

deep waters ($< 10^{\circ}\text{C}$ below 400 m). Salinity exhibits comparatively weaker vertical variability, with mean values of 33.28 ± 1.65 PSU in the upper 100 m and only minor differences among layers. The northern region shows the largest salinity range (30.03–35.11 PSU), while variability decreases toward the south. Dissolved oxygen is highest near the surface and declines with depth, with mean concentrations of $169.78 \pm 34.80 \mu\text{mol kg}^{-1}$ in the upper 100 m. Oxygen variability is greatest in the northern region, whereas the southern region exhibits the most stable values.

Seasonal variability further highlights regional differences (Figure 6). Temperatures increase throughout the year in all regions, with consistently higher values in the middle and southern regions. Salinity decreases gradually in the northern region but remains relatively stable in the middle and southern regions. Dissolved oxygen concentrations are lowest and decline over time in the northern region, while remaining consistently higher in the middle and southern regions.

Temperature-salinity-oxygen relationships indicate broader dispersion in the northern region compared to compact clusters in the middle and southern regions (Figure 6d–f). The northern region shows a negative relationship between temperature and oxygen, whereas the middle and southern regions maintain high oxygen levels across a narrower range of temperature and salinity values. Monthly mean temperatures peak in May–June across all regions, with the southern region exhibiting the largest annual range (2.08°C), followed by the middle (1.85°C) and northern regions (1.72°C).

3.3 Current variability and Lagrangian transport in the Malacca Strait and its connectivity

Current velocity exhibits clear regional and temporal variability (Figure 7). The northern region shows the greatest variability throughout the observation period and the highest maximum velocity (1.054 m s^{-1}), with an average speed of 0.121 m s^{-1} . Peak velocities in the northern region occur in early 2022 and again in 2024, while minimum velocities across all regions decrease to $\sim 0.03\text{--}0.04 \text{ m s}^{-1}$ in mid-2022. The middle and southern regions display lower peak velocities, reaching approximately 0.15 m s^{-1} and 0.13 m s^{-1} , respectively.

Vertical profiles indicate a consistent decline in current speed with depth across all regions. At 10 m depth, the northern region records the highest average velocity ($\sim 0.14 \text{ m s}^{-1}$), followed by the middle (0.13 m s^{-1}) and southern (0.09 m s^{-1}) regions. At 150 m depth, velocities decrease to 0.05 m s^{-1} in the northern region, 0.06 m s^{-1} in the middle region, and $\sim 0.03 \text{ m s}^{-1}$ in the southern region. Monthly distributions further highlight regional contrasts (Figure 6b). In January, median velocities are highest in the northern region (0.15 m s^{-1}) and lowest in the southern region ($\sim 0.08 \text{ m s}^{-1}$). Minimum median velocities

occur in June–July across all regions, with the southern region reaching values near 0.03 m s^{-1} . Current direction also varies regionally (Figure 6c–e), with the middle region exhibiting a more eastward mean direction (136.2°) compared to the northern (166.0°) and southern (154.9°) regions. The middle region shows the most stable current behavior, while the southern region exhibits the greatest directional variability.

Particle-tracking simulations reveal two dominant transport pathways in the Malacca Strait (Figure 8). Particles released in the southeastern Strait are transported southeastward toward the Java Sea, reaching the Bangka Strait within 14–35 days, depending on proximity to the Sumatran coast. In contrast, particles released in the northwestern Strait predominantly follow a northwestward pathway toward the Andaman Sea, reaching it within approximately 28–62 days. Some trajectories exhibit prolonged recirculation within the Malacca Strait and the Andaman Sea before exiting into the Indian Ocean.

At interannual timescales, particle trajectories in the Indian Ocean show progressive southward expansion, with southernmost positions extending to $\sim 33.5^{\circ}\text{S}$ by 2022–2024. While circulation patterns vary among years, trajectories generally remain confined within similar longitudinal ranges, with alternating eastward and westward pathways developing in later years.

3.4 Changes during IOD

In general, the annual range of the IOD is 0.578, reflecting a substantial shift in dipole conditions during the study period. Overall, correlations between the IOD and most parameters are weak (Figure 9). Temperature shows no significant correlation with IOD in any region, with weak and statistically insignificant relationships in the northern ($r = 0.332$, $p = 0.292$), middle ($r = 0.340$, $p = 0.279$), and southern regions ($r = -0.008$, $p = 0.980$). In contrast, salinity in the northern region exhibits a significant positive correlation with IOD ($r = 0.617$, $p = 0.032$), while correlations in the middle ($r = 0.528$, $p = 0.078$) and southern regions ($r = -0.176$, $p = 0.585$) are weaker or negligible.

Oxygen concentrations show strong seasonal variability, most pronounced in the southern region, which exhibits an annual range of $44.58 \mu\text{mol m}^{-3}$, with a maximum in April (mean: $203.88 \mu\text{mol m}^{-3}$) and a minimum in October (mean: $159.30 \mu\text{mol m}^{-3}$). The northern and middle regions show more moderate oxygen variability, with peak values occurring in June ($167.59 \mu\text{mol m}^{-3}$ and $181.45 \mu\text{mol m}^{-3}$, respectively) and minima in October ($131.70 \mu\text{mol m}^{-3}$ and $141.82 \mu\text{mol m}^{-3}$, respectively). Moderate but statistically insignificant positive correlations between oxygen and IOD across all regions suggest that oxygen variability is primarily driven by factors other than IOD.

Salinity exhibits the most consistent response to IOD phase variability across the study regions. During IOD+ phases, volume transport increases by 7.02% in the south-

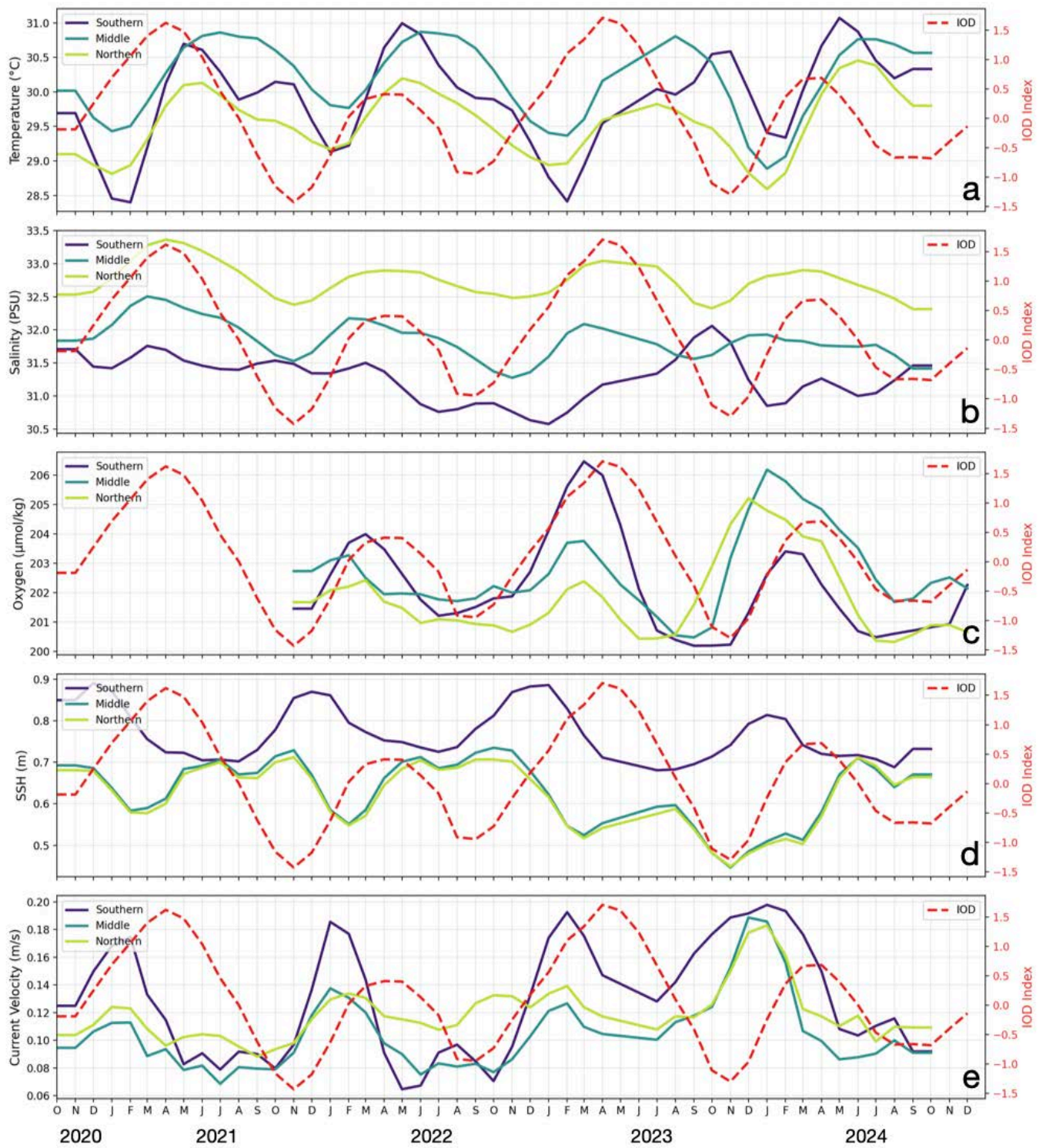


Figure 9. Oceanographic parameters: a) temperature, b) salinity, c) oxygen, d) SSH, and e) currents with IOD index (red dashed line) in the northern region (green lines), middle region (blue lines), and southern region (purple lines).

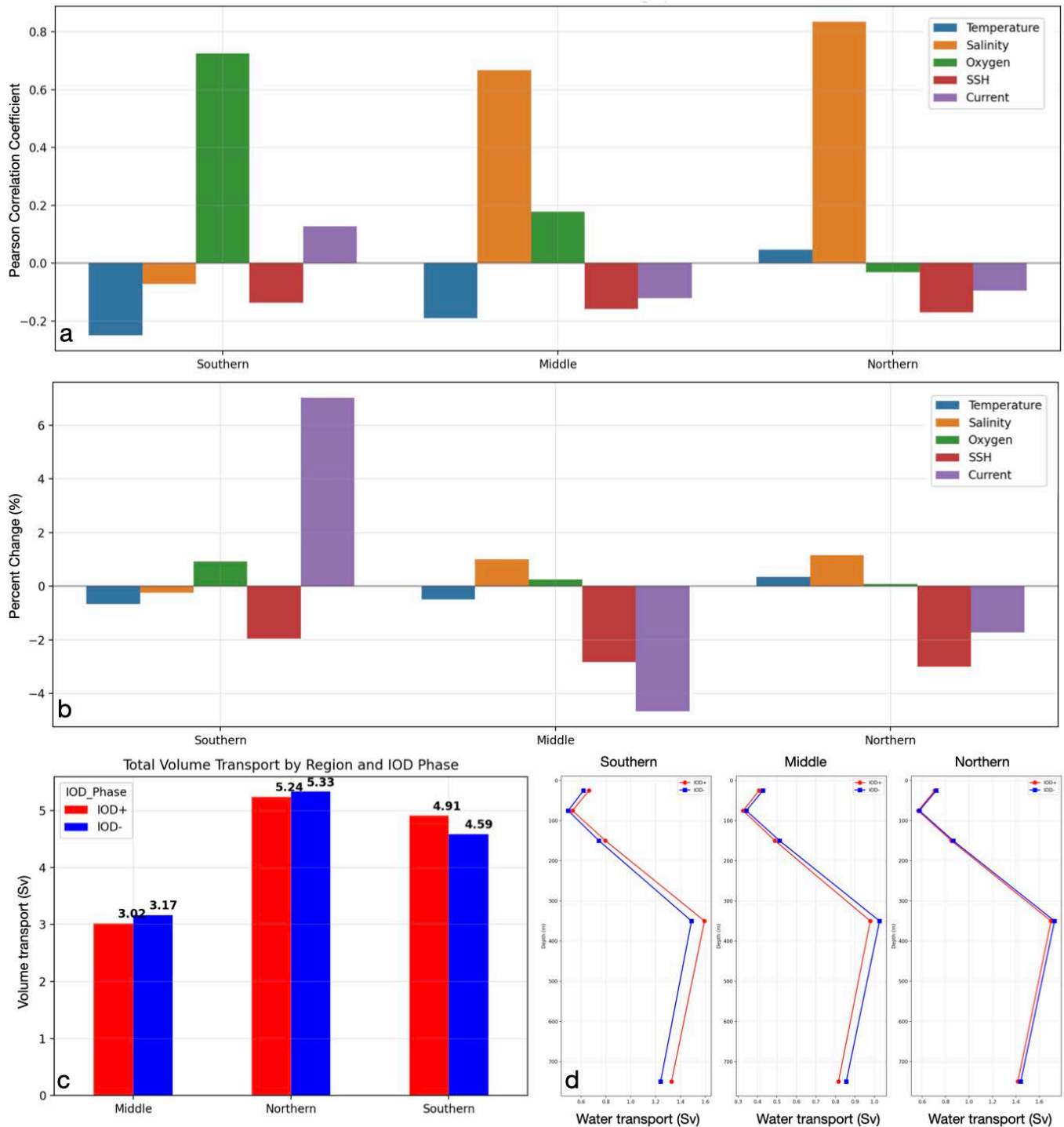


Figure 10. Correlation between oceanographic conditions and volume transport with IOD phase: a) Pearson correlation, b) percent change, c) volume transport in different IOD, d) volume transport in the water column.

ern region, while decreases of 4.66% and 1.72% are observed in the middle and northern regions, respectively (Figure 10). These IOD-related changes in volume transport are evident throughout the water column, with transport magnitude decreasing with depth.

Salinity levels are elevated in the middle and northern regions during IOD+ phases (Figure 10a–b), indicating a positive association with the IOD index. In the southern region, oxygen concentrations increase during IOD+ phases, whereas temperature, sea surface height, and current velocity show no statistically significant differences between IOD+ and IOD– phases. Volume transport profiles further highlight regional contrasts: transport is consistently enhanced at all depths in the southern region during IOD+ phases, while reduced transport is observed throughout the water column in the middle and northern regions.

Total volume transport integrated over depth confirms these regional differences (Figure 10c). The southern region shows a 7.02% increase in transport during IOD+ phases, whereas the middle and northern regions experience reductions of 4.66% and 1.72%, respectively. Although transport intensity decreases with depth in all regions, the vertical coherence of these changes indicates a consistent IOD influence within each regional water column (Figure 10d).

4. Discussion

The vertical stratification of water masses in the Malacca Strait exhibits a distinct north-south gradient. The surface water content diminishes progressively from north to south, while the percentage of deep water increases from 28.9% to 50.1%, and reaches 66.2% in the southern region. The higher proportion of surface and intermediate waters in the northern Malacca Strait reflects enhanced tidal mixing and direct exchange with the Andaman Sea, whereas the dominance of deep water in the southern region indicates restricted vertical interaction and stronger density stratification. This contrast underscores the role of strait geometry and external basin connectivity in controlling vertical structure (Figure 3). The northern region displays a more gradual vertical transition, indicating vertical mixing potentially attributable to intensified tidal forces or interactions with external water masses (Daryabor et al., 2015; Kok et al., 2021). This behavior is consistent with narrow strait dynamics, where strong tidal energy and bathymetric constriction enhance vertical exchange and weaken stratification. The middle zone exhibits characteristics intermediate between the two extremes. Intermediate water is predominantly found in the northern region (5.5%), decreases markedly in the middle region (0.4%), and is virtually absent in the southern region, indicating stronger vertical mixing in the north and more restricted vertical interaction in the south (Ibrahim and Yanagi, 2006; Sangmanee et al., 2020). These findings support the con-

ceptual framework that tidal mixing dominates the northern MST, while buoyancy-controlled stratification prevails in the southern region.

The temperature profiles in the three sections of the MST exhibit distinct thermal characteristics. Elevated salinity and reduced oxygen in the north confirm persistent influence from Andaman Sea waters, while warmer and fresher conditions in the south reflect inputs from the Java Sea and South China Sea. The middle region consistently exhibits transitional properties, confirming its role as a dynamic mixing corridor rather than a passive conduit (Figure 4a). The southern section experiences the most pronounced seasonal temperature fluctuations, whereas the northern and middle regions maintain relatively stable thermal conditions year-round (Roseli et al., 2015). The middle region exhibits the highest temperatures, while the southern region shows comparatively cooler conditions. This contrast reflects differences in surface heat fluxes and freshwater influence, which modulate stratification strength and vertical heat redistribution. Seasonal climatology indicates SST increases of 1 to 2°C during the SWM due to enhanced solar radiation and reduced wind intensity (Isa et al., 2020), whereas in the NEM leads to lower SST associated with stronger winds and precipitation (Akhir and Yong Jaw, 2011).

The vertical temperature profile reveals minimal variation in the upper 30 m, followed by the development of a pronounced thermocline beginning near 30 m and intensifying below 100 m. The persistence of these layers limits vertical oxygen replenishment below 100 m and explains the observed subsurface oxygen decline. This vertical decoupling indicates that biogeochemical variability is tightly linked to physical stratification rather than surface forcing alone (Figure 5a). Temperatures decrease to approximately 19°C at greater depths, indicating a well-defined thermocline between 50 and 100 m separating the warmer surface layer from the cooler subsurface waters (Rizal et al., 2012). Below 100 m, temperatures remain relatively stable with limited seasonal variability, reflecting reduced influence from surface forcing. Such vertical thermal structure is characteristic of tropical straits, where strong surface heating and limited deep mixing maintain persistent stratification. Stratification intensifies during the Northwest Monsoon (NWM) due to surface cooling, while tidal activity enhances mixing in shallower regions (Amiruddin et al., 2011; Sangmanee et al., 2020).

Salinity in the Malacca Strait exhibits strong regional and seasonal variability (Figure 4b; Figure 5b). The northern region consistently records the highest salinity, associated with saline water inflow from the Andaman Sea (Ibrahim et al., 2006). A pronounced halocline develops between 50 and 120 m, marking a transition from fresher surface waters to saltier subsurface layers (Amiruddin et al., 2011; Rizal et al., 2012; Sangmanee et al., 2020). The persistence of this halocline suggests limited vertical

exchange across density layers, reinforcing stratification-driven control of water-mass structure. The southern region exhibits lower salinity, influenced by freshwater inputs from adjacent seas and river discharge. During the NWM, low-salinity waters from the South China Sea enter the strait, while increased river runoff during the Southwest Monsoon further reduces surface salinity. Numerical calculations from previous findings indicated that the Malacca Strait accounts for roughly 43.8% of the yearly freshwater export from the Sunda Shelf (Daryabor et al., 2015).

Dissolved oxygen distribution shows pronounced spatial and seasonal variability (Figure 4c; Figure 5c). The northern region exhibits wider oxygen variability and generally lower concentrations, while the southern region records the highest and most stable oxygen levels. Surface waters remain well oxygenated (4.0–4.7 ml/l), particularly in the northern Strait due to mixing with oxygen-rich Andaman Sea waters (Amiruddin et al., 2011). Oxygen concentrations decline below 100 m as stratification limits vertical exchange and biological consumption increases (Rizal et al., 2012). This vertical oxygen depletion pattern reflects classic stratification-ventilation balance, where restricted mixing suppresses oxygen renewal at depth. During the Northeast Monsoon, oxygen levels increase due to enhanced inflow from the Andaman Sea, whereas summer stratification reduces oxygen replenishment (Wibowo et al., 2022; Jin et al., 2023).

The broader temperature-salinity envelope in the northern region (Figure 6) reflects episodic intrusion of oceanic waters and stronger seasonal modulation. The northern region shows stronger oceanic influence during the SEM and enhanced stratification during the NEM, while the middle and southern regions maintain narrower ranges and higher oxygen levels, likely influenced by river inputs and vertical mixing. Oxygen sensitivity to temperature is most pronounced in the northern region. This indicates a tighter coupling between thermohaline structure and biogeochemical processes in the northern MST. Ocean current patterns exhibit strong spatial and temporal variability across the Malacca Strait (Figure 7a–e). Stronger and more coherent currents in the northern strait reflect direct Andaman Sea forcing, whereas weaker and fragmented currents in the south highlight bathymetric constraints and tidal modulation. These contrasts control regional exchange efficiency and particle pathways. Current velocities and directions are influenced by monsoonal forcing, bathymetry, and external inflows (Ai et al., 2024). The southern region experiences episodically stronger currents, whereas the middle region shows more stable flow throughout the year. During the Northeast Monsoon, southerly currents transport cooler, oxygenated waters from the Andaman Sea, while the Southwest Monsoon reverses flow direction (Daryabor et al., 2016). A north-south gradient is evident, with more coherent northeast-

erly flow in the north and weaker, less organized currents in the south. Such circulation asymmetry is typical of elongated straits subject to competing monsoonal pressure gradients. Tidal forcing, particularly the M2 constituent, further modulates circulation and enhances mixing in shallow areas, while deeper regions remain more strongly stratified (Amiruddin et al., 2011; Rizal et al., 2012).

Unlike previous studies that focus primarily on basin-scale SST anomalies, our results demonstrate that IOD forcing produces spatially heterogeneous hydrographic and transport responses within the Malacca Strait. In particular, the enhancement of southern volume transport during positive IOD phases, in contrast to reduced transport in the middle and northern regions, reveals a region-specific dynamical adjustment that has not been previously quantified. Salinity exhibits the strongest and most spatially coherent response to IOD variability, particularly in the northern region, indicating enhanced control by remote Indian Ocean forcing rather than local atmospheric processes. In contrast, the weak and statistically insignificant temperature correlations suggest that thermal variability in the Malacca Strait is primarily governed by monsoonal forcing and surface heat fluxes rather than direct IOD modulation (Figure 9). Positive IOD phases are associated with elevated SST and reduced dissolved oxygen, particularly in the northern region, suggesting enhanced stratification. These responses align with basin-scale atmospheric anomalies during IOD+ events, which suppress precipitation and reduce freshwater input. Salinity becomes more spatially uniform during IOD+ phases, consistent with reduced freshwater input.

In contrast, negative IOD phases correspond to cooler, fresher, and more oxygenated conditions, especially in the middle and southern regions. The statistically significant increase in volume transport in the southern region during positive IOD phases highlights intensified exchange with the Java Sea, whereas reduced transport in the northern and middle regions suggests a weakening of throughflow toward the Andaman Sea. This pattern indicates that IOD forcing reorganizes circulation pathways rather than uniformly strengthening the Malacca Strait Throughflow (Figure 10). Transport increases by 7.02% in the southern region during IOD+ phases, while the middle and northern regions experience reductions of 4.66% and 1.72%, respectively, indicating region-specific circulation responses. These contrasting responses highlight the MST's sensitivity to large-scale circulation and its role as a dynamically modulated inter-basin connector. However, as the Malacca Strait is a narrow and shallow strait known to be strongly affected by tidal and monsoon-driven processes, its hydrography is widely recognized to be dominated by energetic local dynamics.

5. Conclusion

The hydrography of the Malacca Strait exhibits a complex vertical structure resulting from the dynamic interplay of monsoonal influences, regional mixing, and stratification. A pronounced north-south gradient is evident, with surface water fractions decreasing from 65.6% in the north to 33.8% in the south, while deep-water contributions increase from 28.9% to 66.2%, respectively. The northern region is characterized by higher salinity (32.73 ± 1.39 PSU), lower dissolved oxygen ($161.78 \pm 66.01 \mu\text{mol m}^{-3}$), and stronger stratification, reflecting the influence of dense Andaman Sea inflow and limited vertical exchange. In contrast, the southern region exhibits warmer and fresher waters (31.14 ± 0.88 PSU) with consistently higher oxygen concentrations ($197.11 \pm 26.61 \mu\text{mol}^{-3}$), indicating enhanced ventilation driven by tidal mixing and freshwater inputs. A distinct thermocline between 30 and 100 m, intensifying during the Northeast Monsoon, while a seasonal halocline forms between 50 and 120 m, particularly in the northern strait. Salinity profiles indicate a seasonal halocline, particularly in the northern region, influenced by monsoon-induced circulation and freshwater influx. The middle region functions as a transitional area, embodying both oceanic and coastal influences. The distribution of oxygen reflects stratification patterns, with diminished concentrations in the north and heightened, more stable levels in the south. The impact of IOD phases further modulates these hydrographic patterns: positive IOD events result in warmer, saltier, and more stratified waters, particularly in the north, whereas negative IOD conditions promote fresher, cooler, and more oxygenated waters, mostly in the south. Lagrangian analysis reveals bifurcated circulation pathways toward the Andaman Sea and Java Sea, with volume transport increasing by 7.02% in the southern region during IOD+ phases, while decreasing by 4.66% and 1.72% in the middle and northern regions, respectively. These quantitative results demonstrate the spatially heterogeneous response of the Malacca Strait Throughflow to monsoonal and climate-mode forcing, underscoring its sensitivity to regional and large-scale climate variability. Future studies should integrate in-situ observations to validate model results and better resolve vertical mixing processes in the Malacca Strait. Long-term monitoring is needed to assess the impacts of increasing IOD and monsoon variability. The strong north-south contrasts identified here highlight the need for region-specific management and monitoring strategies.

Acknowledgments

This research was financially supported by Universitas Padjadjaran, Indonesia, through institutional research funding. We would also like to express sincere gratitude to the KomitmenX Research Group team for their valuable assistance and support in data analysis. The bathymetry data

is provided by www.gebco.net.

Conflict of interest

None declared.

References

- Ai, L., Liu, S., Cong, S., Zhang, H., Cao, P., Wu, K., Ye, W., Mohamed, C. A. R., Shi, X., 2024. *Spatial Variability Of Surface Sediments In The Malacca Strait And Its Implications For Sedimentary Environments*. J. Asian Earth Sci. 259, 105922. <https://doi.org/10.1016/j.jseaes.2023.105922>
- Akhir, M. F. M., Yong J., 2011. *Seasonal Variation of Water Characteristics During Inter-Monsoon Along the East Coast of Johor*. J. Sustainability Sci. Manage. 6(2), 206–214.
- Amiruddin, M. A., Zaiton Ibr, Z., Aizat Isma, S., 2011. *Water Mass Characteristics in the Strait of Malacca Using Ocean Data View*. Res. J. Environ. Sci. 5(1), 49–58. <https://doi.org/10.3923/rjes.2011.49.58>
- Chen, H., Malanotte-Rizzoli, P., Koh, T. Y., Song, G., 2014. *The Relative Importance Of The Wind-Driven And Tidal Circulations In Malacca Strait*. Cont. Shelf Res. 88, 92–102. <https://doi.org/10.1016/j.csr.2014.07.012>
- Daryabor, F., Ooi, S. H., Samah, A. A., Akbari, A., 2016. *Dynamics Of The Water Circulations In The Southern South China Sea And Its Seasonal Transports*. Plos ONE 11(7), 1–20. <https://doi.org/10.1371/Journal.Pone.0158415>
- Daryabor, F., Samah, A. A., Ooi, S. H., Chenoli, S. N., 2015. *An Estimate Of The Sunda Shelf And The Strait Of Malacca Transports: A Numerical Study*. Ocean Sci. Discus. 12(1), 275–313. <https://doi.org/10.5194/osd-12-275-2015>
- Haditjar, Y., Putri, M. R., Ismail, N., Muchlisin, Z. A., Rizal, S., 2019. *Numerical Simulation Of Currents And Volume Transport In The Malacca Strait And Part Of The South China Sea*. Eng. J. 23(6), 129–143. <https://doi.org/10.4186/Ej.2019.23.6.129>
- Ibrahim, Z. Z., Yanagi, T., 2006. *The Influence Of The Andaman Sea And The South China Sea On Water Mass In The Malacca Strait*, La Mer, 33–42.
- Isa, N. S., Akhir, M. F., Khalil, I., Kok, P. H., Roseli, N. H., 2020. *Seasonal Characteristics Of The Sea Surface Temperature And Sea Surface Currents Of The Strait Of Malacca And Andaman Sea*. J. Sustainability Sci. Manage. 15(4), 66–77. <https://doi.org/10.46754/jssm.2020.06.007>
- Jin, S., Nie, X., Wang, G., Teng, F., Xu, T., 2023. *Analysis Of The Distribution And Seasonal Variability Of The South China Sea Water Masses Based On The K-Means Cluster Method*. J. Mar. Sci. Eng. 11(3). <https://doi.org/10.3390/jmse11030485>

- Khoirunnisa, H., Wisna, U. J., Lubis, M. Z., 2017. *The Coherency And Correlation Between Sea Surface Temperature And Wind Velocity In Malacca Strait: Cross Wavelet Transform And Wavelet Coherency Application*. JGEET 2(3), 210.
<https://doi.org/10.24273/jgeet.2017.2.3.590>
- Kok, P. H., Wijeratne, S., Akhir, M. F., Pattiaratchi, C., Roseli, N. H., Ali, F. S. M., 2021. *Interconnection Between The Southern South China Sea And The Java Sea Through The Karimata Strait*. J. Mar. Sci. Eng. 9(10).
<https://doi.org/10.3390/jmse9101040>
- Liu, H., Wu, C., Xu, W., Wang, X., Thangaraj, S., Zhang, G., Zhang, X., Zhao, Y., Sun, J., 2020. *Surface Phytoplankton Assemblages And Controlling Factors In The Strait Of Malacca And Sunda Shelf*. Front. Marine Sci. 7, 1–11.
<https://doi.org/10.3389/fmars.2020.00033>
- McDougall, T. J., Barker, P. M., 2011. *Getting Started With TEOS-10 And The Gibbs Seawater (GSW)*, Oceanographic Toolbox Vol. 1.
- Purba, N. P., Pranowo, W. S., Faizal, I., Adiwira, H., 2018. *Temperature-Salinity stratification in the Eastern Indian Ocean using Argo float*. IOP Conf. Ser.: Earth Environ. Sci. 162, 012010.
<https://doi.org/10.1088/1755-1315/162/1/012010>
- Rizal, S., Damm, P., Wahid, M. A., Sündermann, J., Ilhamsyah, Y., Iskandar, T., Muhammad, 2012. *General Circulation in the Malacca Strait and Andaman Sea: A Numerical Model Study*. Am. J. Environ. Sci. 8(5), 479–488.
<https://doi.org/10.3844/ajessp.2012.479.488>
- Roseli, N. H., Akhir, M. F., Husain, M. L., Tangang, F., Ali, A., 2015. *Water Mass Characteristics and Stratification at the Shallow Sunda Shelf of the Southern South China Sea*. Open J. Mar. Sci. 05(04), 455–467.
<https://doi.org/10.4236/ojms.2015.54036>
- Saji, N. H., Goswami, B. N., Vinayachandran, P. N., Yamagata, T., 1999. *A dipole mode in the tropical Indian Ocean*. Nature 401 (6751), 360–363.
<https://doi.org/10.1038/43854>
- Sangmanee, C., Vasinamekhin, V., Khokiattiwong, S., 2020. *Water Characteristic In The South Andaman Shelf Sea From Observations During 2014–2019*. Phuket Mar. Biol. Center Res.Bull.87(77), 75–85.
<https://doi.org/10.14456/Pmbcrb.2020.7>
- Soumya, M., Vethamony, P., Tklich, P., 2015. *Inter-Annual Sea Level Variability in the Southern South China Sea*. Global Planet. Change 133, 17–26.
<https://doi.org/10.1016/j.gloplacha.2015.07.003>
- Webster, P. J., Moore, A. M., Loschnigg, J. P., Leben, R. R., 1999. *Coupled ocean-atmosphere dynamics in the Indian Ocean during 1997–98*. Nature 401, 356–360.
<https://doi.org/10.1038/43848>
- Wibowo, M. A., Tanjung, A., Rifardi, E. M., Yoswaty, D., Susanti, R., Muttaqin, A. S., Fajary, F. R., Anwika, Y. M., 2022. *Understanding The Mechanism Of Currents Through The Malacca Strait Study Case 2020–2022: Mean State, Seasonal And Monthly Variation*. IOP Conference Series. Earth Environ. Sci. 1118(1).
<https://doi.org/10.1088/1755-1315/1118/1/012069>